Palaeogeography, Palaeoclimatology, Palaeoecology 578 (2021) 110578

Contents lists available at ScienceDirect

Palaeogeography, Palaeoclimatology, Palaeoecology

journal homepage: www.elsevier.com/locate/palaeo

Invited Research Article

Isotopic fingerprints of mountain uplift and global cooling in paleoclimatic and paleoecological records from the northern Tibetan Plateau

Mingqiu Hou, Guangsheng Zhuang *, Minghao Wu

Department of Geology and Geophysics, Louisiana State University, Baton Rouge, Louisiana 70803, USA

ARTICLE INFO

Editor: Shucheng Xie

Keywords:
Leaf wax carbon isotopes
Middle-Miocene Climate Optimum
Aridification
Basin isolation
Qilian Shan

ABSTRACT

Post-middle Miocene changes in climate and ecology in the northern Tibetan Plateau have been attributed to tectonic uplift and global climate change. However, the relative roles of tectonism and global climate change have been a long-standing debate. To untangle the complex influences of global climate change versus the tectonism on regional climate and ecology in the northern Tibetan Plateau, we studied carbon isotopes ($\delta^{13}C_{wax}$) of leaf wax long-chain *n*-alkanes and carbon ($\delta^{13}C$) and oxygen isotopes ($\delta^{18}O$) of carbonates from three stratigraphic successions (ca. 16 Ma to 2 Ma) in the Hexi Corridor (foreland basin) and compare them with paleoclimate records in the Qaidam Basin (intermontane basin). Our isotopic results can be divided into two stages. In Stage 1 (16–12 Ma), a decrease of $\delta^{13}C_{wax}$ values in the Hexi Corridor and Qaidam Basin is synchronous with global cooling after the Mid-Miocene Climate Optimum (MMCO). We interpret the 2‰ decrease in $\delta^{13}C_{wax}$ values to be associated with the decline in C_4 plants due to the global cooling. In Stage 2 (since 12 Ma), plant carbon isotope discrimination ($\varepsilon_{CO2\text{-}wax}$) and $\delta^{18}O$ values in the Hexi Corridor reflect relatively stable hydroclimate condition, which contracts with the enhanced aridity in Qaidam Basin during the same interval. We attribute the difference in paleohydrological conditions to the uplift-induced basin isolation and the enhancement of water deficiency in the Qaidam Basin. The effects of late Miocene uplift also manifest as persistent intra-basinal differences in the Hexi Corridor, indicating changes associated with orographic precipitation and ecology.

1. Introduction

Tectonism and global change are two key factors influencing the Cenozoic climate in Asia (Kutzbach et al., 1989; Molnar et al., 1993; An et al., 2001; Dettman et al., 2001; Dettman et al., 2003). The high topography of the Himalaya-Tibetan Plateau orogen was constructed as a result of the India-Asia collision since 50–55 Ma (Tapponnier et al., 2001; Molnar and Stock, 2009; Najman et al., 2010), which in turn changed the regional and global atmospheric circulation patterns (Ruddiman and Kutzbach, 1989; An et al., 2001; Boos and Kuang, 2010; Molnar et al., 2010; An, 2014). High Himalaya-Tibetan Plateau has been proposed to be a primary driver in developing the Asian monsoons (An et al., 2001) and the aridification history of Central Asia (Zhuang et al., 2011; Miao et al., 2012; Li et al., 2016; Wang et al., 2020). On the other hand, global change has impacted the Asian climate throughout the Cenozoic. For example, the Asian interior has become increasingly arid due to global cooling at the Eocene-Oligocene transition (Dupont-Nivet et al., 2007) and the Middle Miocene Climate Maximum (Miao et al., 2011; Tang et al., 2011; Zhuang et al., 2011).

Differentiating the relative role of tectonism versus global climate change remains challenging. We are particularly interested in the middle Miocene, a period of active tectonism when the global climate change also manifests the impact in the regional climatic records. Sedimentary and geochemistry evidence suggest that the northern Tibetan Plateau was uplifted during the late Miocene (Bovet et al., 2009; Zhuang et al., 2014; Zuza et al., 2016; Zhuang et al., 2019). The high topography of the Tibetan Plateau has acted as a moisture barrier of the Westerlies, enhancing the regional aridity in Central Asia (Miao et al., 2012; Wang et al., 2020). However, the dry climate has also been affected by global climate change. Post-Middle Miocene global cooling, one of the most profound climate changes during the Cenozoic, has drawn particular attention in the studies of Central Asian climate because of contemporary uplift of the northern Tibetan Plateau (Bovet et al., 2009; Zhuang et al., 2014; Zuza et al., 2016; Zhuang et al., 2019). Global cooling can reduce moisture load in the atmosphere, limiting the precipitation in Central Asia (Dupont et al., 2007; Miao et al., 2011). Sedimentary records in the Qaidam Basin show increase in xerophytic pollen and increasing carbonate $\delta^{18}O$ values, indicating an extensively

* Corresponding author.
E-mail addresses: mhou1@lsu.edu (M. Hou), gzhuang@lsu.edu (G. Zhuang), mwu7@lsu.edu (M. Wu).

https://doi.org/10.1016/j.palaeo.2021.110578
Received 18 January 2021; Received in revised form 11 June 2021; Accepted 14 July 2021
Available online 20 July 2021

arid climate that is synchronous with global cooling since ca. 15 Ma (Zhuang et al., 2011; Miao et al., 2012).

How tectonic activity and global climate change shaped the regional ecological community has also added complexity to the tectonism-global climate dilemma. In the northern Tibetan Plateau, temperature and hydrological changes invoked by contemporary tectonic uplift have changed the land vegetation since the mid-late Miocene. For example, leaf wax carbon isotopic data from the North Pacific suggest that a decline in C_4 plant proportion during ~12–8 Ma is associated with cold/arid climate due to the rapid growth of source area - northern Tibetan Plateau, as well as the global cooling (Jia et al., 2012). C_4 plant has been recognized to expand globally during the late Miocene-early Pliocene (Cerling et al., 1997; Tipple and Pagani, 2007; Edwards et al., 2010; Strömberg, 2011). C_4 plants preferentially adapt to low latitudes with warm temperature (>25 °C) and sufficient precipitation (>25 mm per month), whereas C_3 plants have a competitive advantage to inhabit high latitudes and high elevations (Collatz et al., 1998; Edwards and Smith, 2010). The declining atmospheric pCO_2 and warm and dry climate favor C_4 grasses relative to C_3 woody plants in tropic and subtropic regions since the middle-late Miocene (Pagani et al., 1999; Huang et al., 2007; Edwards et al., 2010).

In this study, we reconstruct paleoecology and paleoclimate in the Hexi Corridor (foreland basin), then compare with records in the Qaidam Basin (intermontane basin) (Wu et al., 2019). We aim to address two problems: (1) linkage between climate and ecology in the Northern Tibetan Plateau and (2) influence of tectonic uplift on regional climate by comparing paleoclimate records in the Hexi Corridor and Qaidam Basin. The intra- and inter-basinal comparisons advance our understanding of the relative role of tectonism and global cooling on regional climatic and ecological evolutions.

2. Geological background and modern climate

Hexi Corridor (Fig. 1A), an elongate foreland basin in the northern margin of Tibetan Plateau, is constrained by the North Qilian Shan Fault to the south, Altyn Tagh Fault to the west, Alax Block to the north, and Ordos Block to the east. The basin is divided into three sub-basins: Jiuxi, Jiudong, and Zhangye Basins (Dai et al., 2005; Fang, 2005). Our study sites are in the Jiuxi Basin (Fig. 1B) bounded by the North Qilian Shan Fault to the south, Altyn Tagh Fault to the west, Heishan Fault to the north, and Jiayuguan Fault to the east.

Cenozoic sedimentation in the Hexi Corridor mainly consist of five formations: the late Eocene Huoshaogou Formation (ca. 40.2–33.35 Ma), the late Oligocene to early Miocene Baiyanghe Formation, the middle Miocene to Pliocene Shulehe Formation (ca. 13–5 Ma), the Pliocene-Pleistocene Yumen conglomerate (ca. 5–0.9 Ma), and the late Pleistocene Jiuquan conglomerate (ca. 0.9–0.1 Ma) (GBGMR, 1989; Zhao et al., 2001; Dai et al., 2005). We study post-middle Miocene successions in the Laojunmiao (LJM), Wenshushan (WSS), and Caogou (CG) stratigraphic sections in the Jiuxi Basin, western Hexi Corridor (Fig. 2). The ages of each stratigraphic section are constrained by lithostratigraphy, biostratigraphy, and magnetostratigraphy (Zhao et al., 2001; Fang, 2005; Wang et al., 2016).

The LJM section (97°30.7′E, 39°47.5′N) (Fig. 2) extends from the upper Miocene (ca. 13 Ma) to the upper Pleistocene (ca. 0.1 Ma) (Fang, 2005). The LJM section is subdivided into three formations. The lower part of the Shulehe Formation (0–600 m) is composed of sandy siltstone and mudstone, associated with the deep lacustrine environment. The upper part of the Shulehe Formation (600–1200 m) is dominated by sandy conglomerates interbedded with muddy sandstone, deposited in shallow lacustrine to fan delta environments. Yumen Conglomerate and Jiuquan Conglomerate (1200–2000 m) consist of poorly sorted gravels associated with an alluvial fan environment.

The WSS section (98°19.4′E, 39°40.4′N) (Fig. 2) spans from the late Miocene (ca. 11.5 Ma) to the late Pleistocene (> 0.9 Ma) (Zhao et al., 2001). The WSS section is subdivided into three formations. The lower Shulehe Formation (0–260 m) consists of siltstone and medium to coarse sandstone, channel lag deposits above the erosional surface. The upper

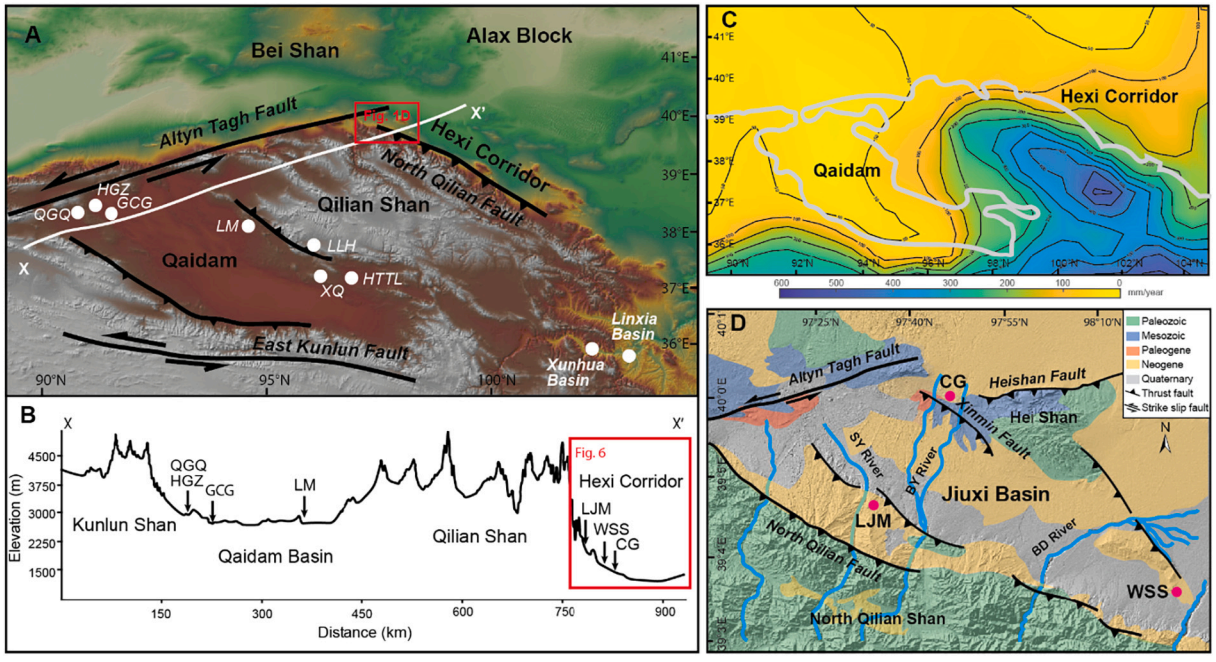

Fig. 1. A, Topography of northern Tibetan Plateau, showing major faults, locations of paleoclimate studies from stable isotopes of fluvial and lacustrine carbonates, and leaf wax lipids. HGZ: Honggouzi (Wu et al., 2019); HTTL: Huaitoutala (Zhuang et al., 2011); Linxia Basin and Xunhua Basin (Hough et al., 2011); Qigequan (QGQ), Ganchaigou (GCG), Lake Mahai (LM), Lulehe (LLH), and Xiao Qaidam (XQ) are from (Kent-Corson et al., 2009). B, Elevation profile of Qaidam Basin, Qilian Shan, and Hexi Corridor, with nearby paleoclimate study sites. C, modern precipitation in the northern Tibetan Plateau, with gray line denoting 3000 m contour. D, Geological map of Jiuxi Basin (modified from GBGMR, 1989 and Wang et al., 2016), showing major faults, strata, and studied sedimentary sections: Caogou (CG), Laojunmiao (LJM), and Wenshushan (WSS).

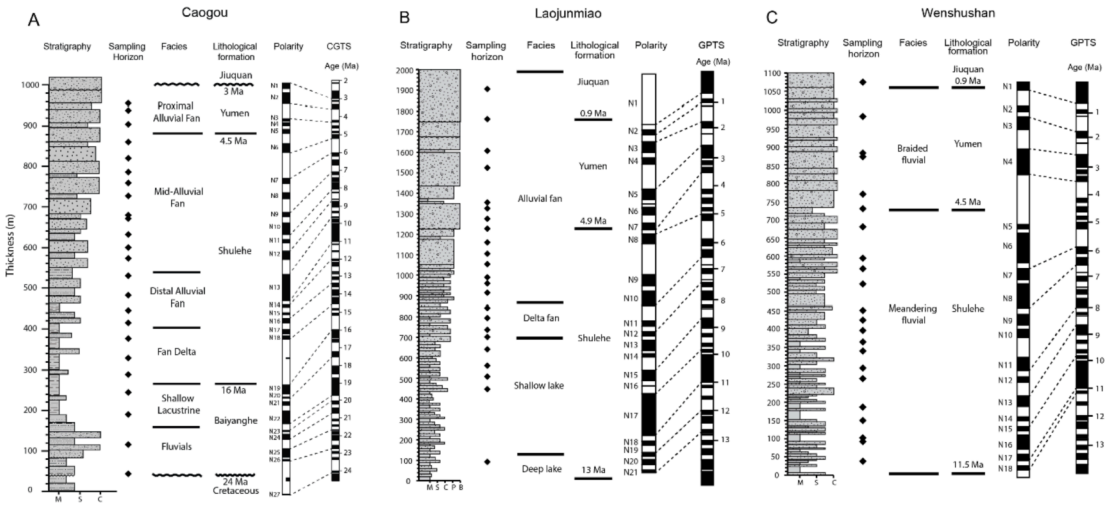

Fig. 2. Stratigraphic column of A, Caogou (CG), B, Laojunmiao (LJM), and C, Wenshushan (WSS) sections with the interpretation of depositional facies and lithological Formations. Age constraints for CG, LJM, and WSS sections are from Wang et al. (2016), Fang (2005), and Zhao et al. (2001). M: mudstone; S: sandstone; C: conglomerate; P: pebble; B: boulder.

Shulehe Formation (260–750 m) has increasing proportions of medium-coarse sandstone and sandy conglomerate, deposited in the meandering fluvial environment. Yumen Conglomerate and Jiuquan Conglomerate (750–1150 m) are composed of pebble conglomerate interbedded with coarse sandstone, which is interpreted as the braided fluvial deposits.

The CG section (97°46.6′E, 40°00.2′N) (Fig. 2) spans from the late Oligocene (ca. 24.2 Ma) to the late Pliocene (2.8 Ma) (Wang et al., 2016) and is subdivided into five depositional units. The lower Baiyanghe Formation (0–170 m) is composed of fine to coarse sandstone with pebble conglomerate on the erosional surface. This unit is characterized by upward-fining trends, channel lag deposits, and cross-stratification, which is associated with a braided fluvial environment. The upper Baiyanghe Formation (170–280 m) comprises mudstone and interbedded fine sandstone and siltstones, reflecting a shallow lacustrine environment. The lower Shulehe Formation (280–530 m) is dominated by fine sandstone and siltstone, reflecting the delta fan environment. Upper Shulehe Formation (530–800 m) consists of pebble to cobble conglomerate with minor sandstone and siltstone layers. The upward coarsening and coarse-grained size are interpreted to be distal and middle alluvial fan environments. Overlying Yumen Conglomerate (800–1050 m) is primarily composed of pebble- to cobble-conglomerate, reflecting a proximal alluvial fan environment.

The northern Tibetan Plateau is mainly interacted by two moisture sources: Westerlies and Asian summer monsoon. Hexi Corridor on the northern margin of Tibetan Plateau predominately receives Atlantic moisture from the Westerlies and regionally recycled surface water (Araguás-Araguás et al., 1998; Li and Garzione, 2017). The summer monsoons (East Asian summer and South Asian summer monsoon) could only influence the southeastern margin of the Plateau (Araguás-Araguás et al., 1998; Tian et al., 2001). The modern Hexi Corridor receives the Westerlies moisture all year round with a substantial amount of recycled surface water from inner Asia (Bershaw et al., 2012; Li and Garzione, 2017). The meteorological data from International Atomic Energy Agency (IAEA) station in Zhangye show that the average annual precipitation falls in ~100–150 mm, with ~95% of precipitation occurring during summer; average temperature ranges from −10 °C to 25 °C, with the average annual temperature at 8 °C (IAEA/WMO, 2006).

3. Methods and materials

We studied leaf wax $\delta^{13}C_{wax}$ values of mudstone and siltstone from three stratigraphic sections in Jiuxi Basin, including 23 samples from the LJM section, 21 samples from the WSS section, and 15 samples from the CG section. $\delta^{13}C_{wax}$ values of terrestrial-higher plants are a function of $\delta^{13}C$ of atmospheric CO_2 ($\delta^{13}C_{atm}$) and photosynthetic fractionation during carbon fixation (Farquhar et al., 1982; Farquhar et al., 1989a; Sparks and Ehleringer, 1997). Fractionation between $\delta^{13}C_{atm}$ and $\delta^{13}C_{wax}$, expressed by carbon isotope discrimination ($\varepsilon_{CO2\text{-}wax}$), is modulated by the physiological (photosynthetic pathways) and environmental factors (e.g., water stress) (Farquhar et al., 1982; Sparks and Ehleringer, 1997; Diefendorf and Freimuth, 2017). $\varepsilon_{CO2\text{-}wax}$ is calculated with given $\delta^{13}C_{atm}$ values:

$$\varepsilon_{CO2-wax} = \left(\frac{\delta^{13}C_{atm}+1}{\delta^{13}C_{wax}+1} - 1\right) \times 10^3 \quad (1)$$

We also analyzed oxygen and carbon isotopic composition ($\delta^{18}O$ and $\delta^{13}C$) of bulk sediments from LJM, WSS, and CG sections, to study changes in paleoclimate conditions, such as precipitation, evaporation, and temperature.

3.1. Total lipid extraction

Rock samples were broken and grounded with pestle and mortar into the coarse-sand size and freeze-dried for 48 h before extraction. Total lipids were extracted with Soxhlet extractor using the azeotrope of dichloromethane/methanol (DCM/MeOH; 2:1 *v*/v) for 48 h. The lipid extracts were evaporated under a stream of pure nitrogen until dry. Organic compounds in total lipid extracts were separated into apolar, intermediate, and polar fractions using a pipette column filled with ca. 0.5 g of activated silica gel and eluted with 2 ml hexane, 4 ml DCM and 4 ml methanol sequentially.

3.2. Column chromatography and n-alkanes characterization

n-Alkanes contained in the apolar fractions are re-dissolved into 1500 μl of hexane. *n*-Alkane abundances were determined using a Thermal Trace 1310 Gas chromatography (GC)-flame ionization detector (FID) fitted with programmable-temperature vaporization (PTV) injector and TG-1MS column (60 m long, 0.25 mm i.d., 0.25 μm film thickness). Samples were carried by helium at a rate of 2 ml/min. GC oven temperature is ramped from 60 °C (holding for 1 min) to 320 °C at a rate of 15 °C/min (holding for 20 min). Individual *n*-alkanes were identified by comparing the elution time with a reference standard (Mix A6, Schimmelmann, Indiana University Bloomington).

The carbon preference index (CPI) of *n*-alkanes were determined using the equation:

$$CPI = \frac{1}{2}\frac{\sum A(23+25+27+29+31+33)+\sum A(25+27+29+31+33+35)}{\sum A(24+26+28+30+32+34)} \quad (2)$$

Where A stands for the areas of the individual *n*-alkanes, identified by chromatography analysis using Xcalibur software. The numbers (23–35) represent the chain length of *n*-alkanes.

3.3. Leaf wax carbon isotopic analysis

Leaf wax carbon isotopic values were measured using Trace 1310 GC coupled to a Thermo Delta V Advantage isotope ratio mass spectrometer (IRMS) with a Thermo Isolink interface. Trace 1310 GC is fitted with a PTV injector and TG-5MS column (30 m long, 0.25 mm i.d., 0.25 μm film thickness). Samples were carried by helium at a rate of 2 ml/min. Compounds were separated by the GC with the temperature ramping from 60 °C (held for 2 min) to 170 °C at 14 °C/min, to 300 °C at 3 °C/min, to 320 °C at 14 °C/min, then isothermally holding at 320 °C for 5 mins. Samples were analyzed in duplicate with a mean analytical precision of 0.1‰ for $\delta^{13}C$. The *n*-alkane reference materials Mix A6 (nC_{16} to nC_{30}; Arndt Schimmelmann, Indiana University) were measured every four to six analyses for monitoring the instrumental drift. Carbon isotope ratio values were calibrated relative to Mix A6. $\delta^{13}C$ values of nC_{16-30} alkanes of Mix A6 are −26.15‰, −31.88‰, −32.70‰, −31.99‰, −33.97‰, −28.83‰, −33.77‰, −33.77‰, −32.13‰, −28.46‰, −32.94‰, −30.49‰, −33.20‰, −29.10‰, and − 29.84‰. $\delta^{13}C$ values of *n*-alkanes are reported relative to Vienna Pee Dee Belemnite (VPDB) using the equation:

$$\delta^{13}C = \left(\frac{R_{sample}}{R_{reference}} - 1\right) \quad (3)$$

Where R represents the $^{13}C/^{12}C$ ratios in samples and standard reference materials.

3.4. Calculation of C_4 plant contribution

Plants using C_3 (Calvin-Benson) carbon fixation pathways have larger carbon isotopic fractionation than those using the C_4 (Hatch-Slack) pathway (O'Leary, 1988; Tipple and Pagani, 2007; Diefendorf and Freimuth, 2017). The modern mean $\varepsilon_{CO2\text{-}wax}$ value of nC_{31} is −26.5 ± 3‰ for C_3 plants, while it is −13.7 ± 2‰ for C_4 plants (Tipple and Pagani, 2010; Jia et al., 2012). We model the change of *n*-alkanes contribution from C_4 plants in the Hexi corridor by assuming that the Miocene $\varepsilon_{CO2\text{-}wax}$ is the same as the modern values. The equation is expressed as follows:

$$\varepsilon_{CO_2-wax} = \varepsilon_{CO_2-C3} \times (1 - f_{c4}) + \varepsilon_{CO_2-C4} \times f_{c4} \quad (4)$$

Where $\varepsilon_{CO2\text{-}C3}$ and $\varepsilon_{CO2\text{-}C4}$ represent the carbon isotopic fractionation between $\delta^{13}C_{atm}$ and $\delta^{13}C_{wax}$ of *n*-alkanes derived from C_3 plants and C_4 plants, respectively. f_{C4} is the fraction of C_4 plants' abundance. $\varepsilon_{CO2\text{-}wax}$ values are calculated with Eq. (1) with reconstructed CO_2 (Tipple et al., 2010) and observed leaf wax carbon isotopes (Fig. 3).

3.5. Oxygen and carbon isotopic analysis of bulk samples

About 0.5–1 mg of powdered bulk rock samples were analyzed for $\delta^{18}O$ and $\delta^{13}C$ values. Samples were grounded by an agate mortar and were dried in the oven at 70 °C for 24 h. Dried samples were reacted with orthophosphoric acid at 72 °C to produce carbon dioxide and water. $\delta^{18}O$ and $\delta^{13}C$ values were measured using a Gas Bench interfaced with Thermo Delta V Advantage IRMS. Isotopic results are reported with respect to VPDB by assigning a $\delta^{18}O$ value of −4.31‰ and a $\delta^{13}C$ value of 2.57‰ to the laboratory standard CMA. The precision of repeated analysis for $\delta^{18}O$ values is less than 0.15‰. The precision of repeated analysis for $\delta^{13}C$ values is less than 0.13‰.

4. Results

Samples from LJM, WSS, and CG sections are most abundant in long-chain *n*-alkane homologs (nC_{27}, nC_{29}, and nC_{31}), indicating a terrestrial higher plant source (Eglinton and Hamilton, 1967; Tipple and Pagani, 2007). CPI values of all sections in the Hexi Corridor are higher than 1, with a mean value of 1.3. We report carbon isotopic compositions of nC_{29} and nC_{31} alkanes from LJM, WSS, and CG sections and discuss their weighted mean values ($\delta^{13}C_{wax}$) in the text (Fig. 3).

$\delta^{13}C_{wax}$ values of CG section (Fig. 3E) decrease from −27.4‰ to −29.3‰ between 15.6 Ma to 10.9 Ma and vary between −29.3‰ and − 29.9‰ from 10.9 Ma to 4.8 Ma. Then isotopic values vary between −31.1‰ and − 29.7‰ from 4.2 Ma to 2.9 Ma. $\delta^{13}C_{wax}$ values of LJM section (Fig. 3E) decrease from −30.5‰ at 12.7 Ma to −31.9‰ at 10.2 Ma, then vary between −30.5‰ and − 33.0‰ from 10.2 Ma to 2.6 Ma. $\delta^{13}C_{wax}$ values of WSS section (Fig. 3E) decrease from −30.1‰ at 11.4 Ma to −31.4‰ at 9.7 Ma, then vary between −30.1‰ and − 32.6‰ from 9.7 Ma to 1.7 Ma.

We divided the $\delta^{13}C_{wax}$ records in Hexi Corridor into two stages by comparing our records with regional paleoclimate records (Fig. 3). Stage 1 (16–12 Ma) shown in CG records is characterized by a decrease in $\delta^{13}C_{wax}$ values by ~2.5‰, consistent with the decreasing trends in

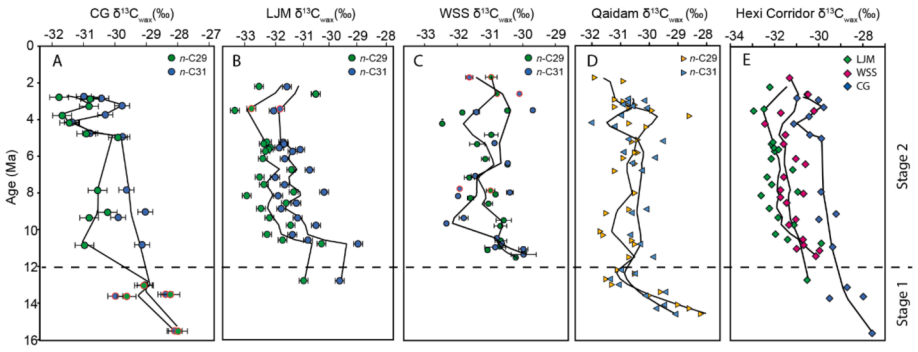

Fig. 3. Leaf wax carbon isotope ($\delta^{13}C_{wax}$) records: (A) Caogou (CG), (B) Laojunmiao (LJM), and (C) Wenshushan (WSS) sections from the Hexi Corridor. Samples with CPI values >1.5 have red outlines. (D) Qigequan (QGQ) and Honggouzi (HGZ) sections from the Qaidam Basin (Wu et al., 2019); (E) Weighted mean $\delta^{13}C_{wax}$ of C_{29} and C_{31} *n*-alkanes in CG, LJM, and WSS sections. Black curves are generated by Loess regression. (For interpretation of the references to colour in this figure legend, the reader is referred to the web version of this article.)

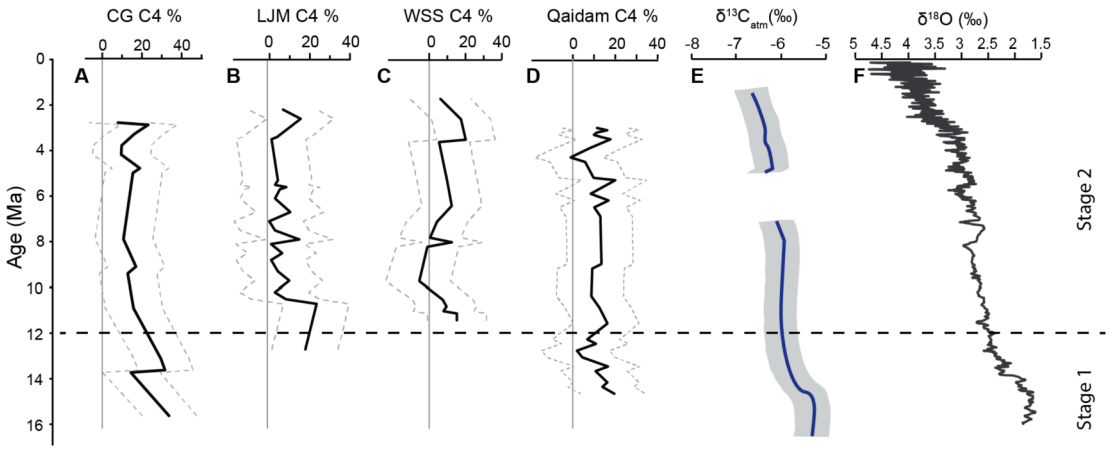

Fig. 4. Calculated C_4 contribution from $\delta^{13}C_{wax}$ of C_{31} *n*-alkanes in the CG (A), LJM (B), and WSS (C) sections from the Hexi Corridor and QGQ and HGZ sections from the Qaidam Basin (D) (Wu et al., 2019). Dashed gray lines denote 1-sigma calculation uncertainty of modern end-members C_{31} *n*-alkanes. E, Reconstructed $\delta^{13}C$ of atmosphere CO_2 ($\delta^{13}C_{atm}$) from benthic foraminifera are shown in blue with a 90% confidence interval (Tipple et al., 2010). F, A compilation of global benthic foraminifera $\delta^{18}O$ records with 20-point moving average (Zachos et al., 2001). (For interpretation of the references to colour in this figure legend, the reader is referred to the web version of this article.)

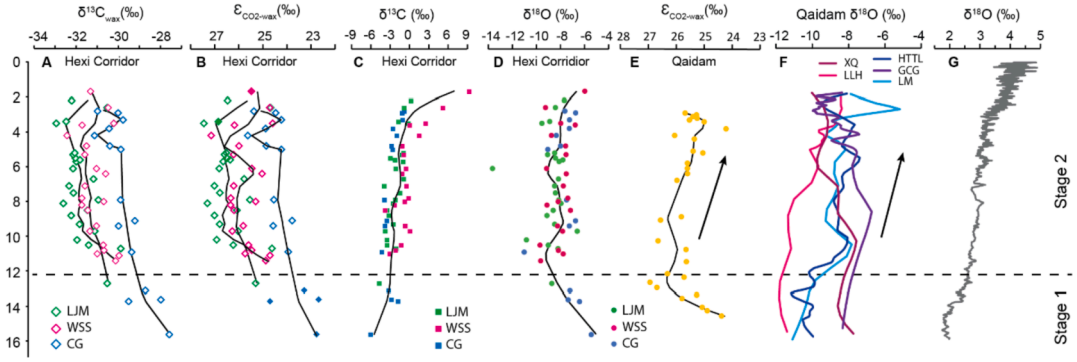

Fig. 5. Comparison of paleoecologic and paleoclimatic records in Northern Tibetan Plateau. A, Weighted mean $\delta^{13}C_{wax}$ values of C_{29} and C_{31} *n*-alkanes in CG, LJM, and WSS sections. B, $\varepsilon_{CO2\text{-}wax}$ values of C_{29} and C_{31} *n*-alkanes in CG, LJM, and WSS sections. Data with CPI values >1.5 are solid filled. Black curves in A and B denote the Loess regression of data in each stratigraphic section. C, $\delta^{13}C$ records of bulk rocks in the CG, LJM, and WSS sections. D, $\delta^{18}O$ records of bulk rocks in the CG, LJM, and WSS sections. Black curves in C and D are generated by Loess regression of all data in the Hexi Corridor. E, $\varepsilon_{CO2\text{-}wax}$ records of HGZ and QGQ in the Qaidam Basin (Wu et al., 2019). F, carbonate $\delta^{18}O$ records from Ganchaigou (GCG), Lake Mahai (LM), Lulehe (LLH), and Xiao Qaidam (XQ) (Kent-Corson et al., 2009) and Huaitoutala (HTTL) (Zhuang et al., 2011). Locations of the paleoclimate studies discussed in the text are shown in Fig. 1. G, A compilation of global benthic foraminifera $\delta^{18}O$ records with 20-point moving average (Zachos et al., 2001).

$\delta^{13}C_{wax}$ records from the Qigequan (QGQ) and Honggouzi (HGZ) sections in the Qaidam Basin (Wu et al., 2019). This stage is concurrent with the positive shift of global benthic foraminifera $\delta^{18}O$ values (Fig. 5G) (Zachos et al., 2001) and declined $\delta^{13}C$ values of atmosphere CO_2 (Fig. 4E) (Tipple et al., 2010). In Stage 2 (since 12 Ma), $\delta^{13}C$ values in LJM, WSS, and CG sections show general decreasing trends.

Carbonate $\delta^{13}C$ and $\delta^{18}O$ records in the Hexi Corridor can be subdivided into two stages (Figs. 5 and 6). Stage 1 (16–12 Ma) is recorded in the CG section and shows a decrease in $\delta^{18}O$ values from −5.4‰ to −11.0‰. In Stage 2 (since 12 Ma), $\delta^{18}O$ values vary between −6.7‰ and − 11.0‰ in CG, between −5.9‰ and − 9.7‰ in WSS, and between −10.8‰ and − 7.6‰ in LJM except one lowest value of −13.6‰ at 6.1 Ma. $\delta^{13}C$ values range from −0.8‰ to −4.3‰ in CG and from 0‰ to −3.9‰ in LJM. $\delta^{13}C$ values of WSS vary between 0 to −3.7‰ from 12 Ma to 4 Ma and then increase up to 10.1‰ after 4 Ma.

5. Discussions

5.1. Distribution of n-alkanes

The modern terrestrial vascular plants have a predominance of odd-carbon numbered *n*-alkanes, with average CPI values greater than 4 (Collister et al., 1994). The average CPI of the Hexi Corridor samples is 1.3 (Fig. S2), which is low than the average CPI (~3.5) of the last glacial sediments in the Qaidam Basin (Hou et al., 2020). CPI values of Hexi samples are within the range of CPI values of the last glacial sediments in the Qaidam Basin (Fig. S2). Several common factors could cause lower CPI in Hexi samples than that in modern sediments: thermal or diagenetic alteration, recycling of old organic matter, and biodegradation.

Long-chain *n*-alkanes may be heated and broken down as sediments are buried and consolidated throughout time (Eglinton et al., 1988). The loss of odd-numbered long-chain *n*-alkanes due to thermal alteration could lower CPI values in sediments (Simoneit, 1994; Diefendorf et al., 2015; Kara-Gülbay et al., 2019; Lu et al., 2021). If the Hexi *n*-alkanes distributions have been thermally modified, we would expect to observe decreasing CPI values with burial depth. However, CPI values of Hexi samples mostly range from 1.0 to 2.0 and do not show a systematic decreasing trend with increasing depth (Fig. S1). We suggest that there is no significant loss of *n*-alkanes during post-depositional thermal alteration. Furthermore, studies on modern leaves reveal that the carbon isotopic composition of *n*-alkanes are constant up to 200 °C and may increase the isotope values by ca. 2‰ between 200 °C and 330 °C

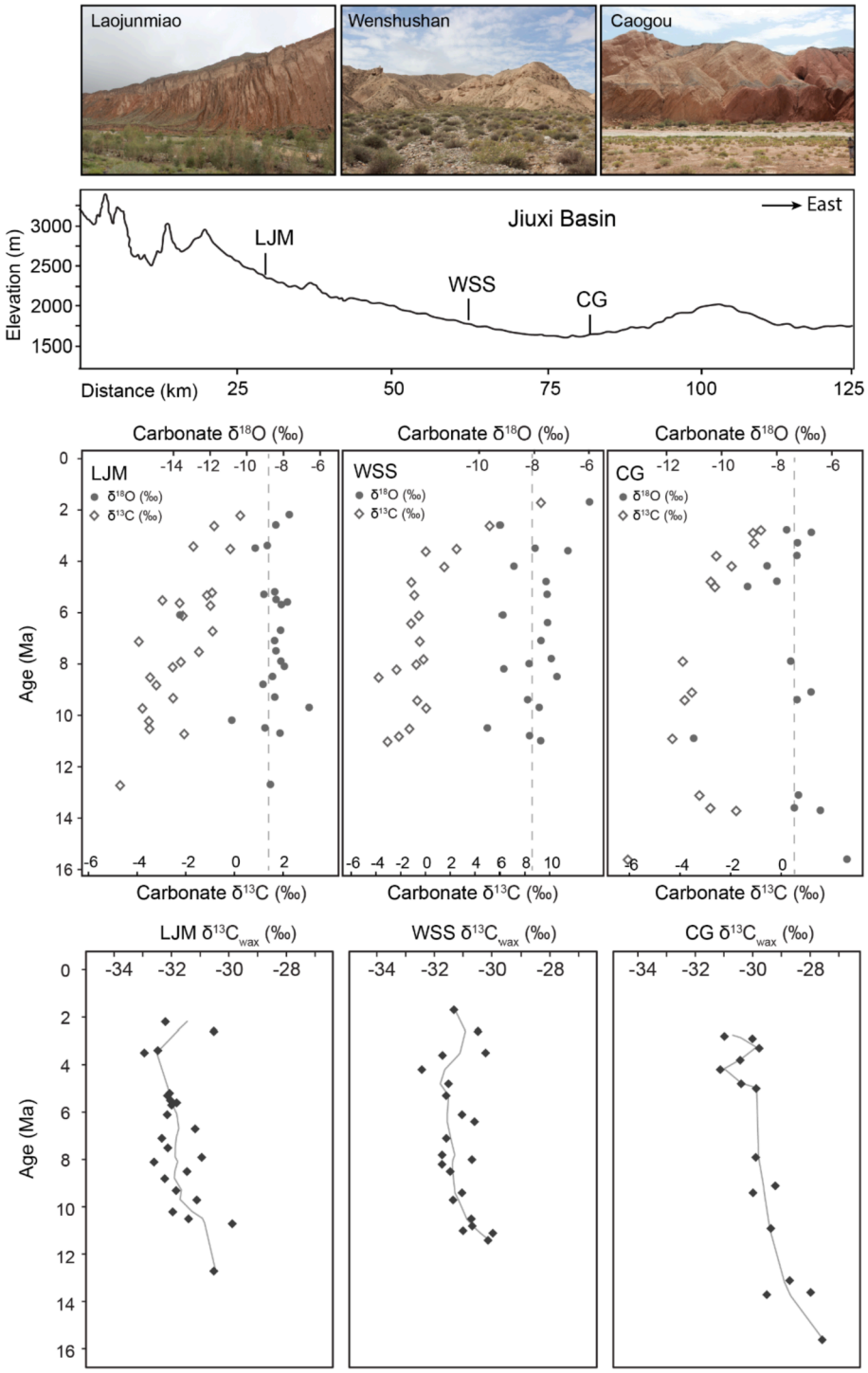

Fig. 6. Field pictures show ecological changes across the elevation transaction in the western Hexi Corridor. Carbonate $\delta^{18}O$ and $\delta^{13}C$ and $\delta^{13}C_{wax}$ records from CG, LJM, and WSS sections. Dashed gray lines denote the mean $\delta^{18}O$ values of each sedimentary section. Solid gray curves are generated by the Loess regression for $\delta^{13}C_{wax}$ data for each stratigraphic section. Refer to Fig. 1 for the localities.

(Diefendorf et al., 2015). The depth of Paleogene stratigraphic succession in the Jiuxi Basin is shallower than 3800 m (An, 1998), which is consistent with the early oil window (equivalent to ca. 100 °C isotherm) (Selley, 1998). Therefore, thermal maturation with a temperature of 100 °C is less likely to affect the $\delta^{13}C_{wax}$ values in the Hexi Corridor.

The northern Tibetan Plateau is characterized by rapid basin-filling since the Oligocene (Metivier et al., 1998). Sediments could be mixed with old organic matter during deposition (Kennicutt II et al., 1987). Old sediments tend to have lower CPI values than the younger sediments because of more intensive degradation and diagenetic impact throughout time. Increasing recycled organic matter of higher thermal maturity may dilute the odd-over-even predominance of *n*-alkanes in the Hexi records. We analyzed the total organic carbon (TOC%) to evaluate the potential influence of old organic materials (Fig. S4). Samples with high TOC% but low CPI values could indicate a substantial input of recycled organic matter. CPI values close to 1 due to recycled organic matter have also been reported in modern drainages (Bakhtiari et al., 2010; Fang et al., 2014; Ankit et al., 2017; Wang et al., 2018). Cross-plot

of CPI values and TOC% in the CG, WSS, and LJM shows no correlation between CPI values and TOC% (Fig. S4). Recycled carbon is unlikely to be the reason for the low CPI values in the Hexi Corridor.

Microbial degradation is another possible factor for low CPI values. Biodegradation can cause low CPI values (Marzi et al., 1993; ChaIneau et al., 1995; Andersson and Meyers, 2012), high content of medium-chain *n*-alkanes ($C_{20–24}$), and decreasing $\delta^{13}C_{wax}$ values (Brittingham et al., 2017). Our samples are less abundant with medium-chain *n*-alkanes. However, we cannot rule out the possible effect of biodegradation on our samples. Given that CPI values in the Hexi Corridor have low variations (< 0.4), this may indicate a relatively constant microbial alteration and most likely have a similar isotopic effect, which is supposed to set up a similar "baseline" for $\delta^{13}C_{wax}$ records. Further investigations are required to quantify the impact of biodegradation to $\delta^{13}C_{wax}$ values.

5.2. Decline in C_4 plant in the northern Tibetan Plateau since middle Miocene global cooling

The most pronounced change in $\delta^{13}C_{wax}$ values occurs in Stage 1 and is recorded by the CG records in samples with CPI values >1.5. The 2.5‰ negative shift of $\delta^{13}C_{wax}$ values, in contrary to the positive shift by the thermal degradation (see Section 5.1), from 16 Ma to 12 Ma reflects a change in carbon isotope discrimination and $\delta^{13}C_{atm}$ compositions. Reconstructed $\delta^{13}C_{atm}$ values that are based on the benthic foraminifera records (Fig. 4E) (Tipple et al., 2010) can explain a ~ 0.6‰ decrease from 16 Ma to 12 Ma. Hence, the ~2‰ difference in $\delta^{13}C_{wax}$ value reflects the change in carbon assimilation in response to a change in plant communities (e.g., C_3 vs. C_4 plants) and water stress. Several scenarios can explain the negative shift in CG $\delta^{13}C_{wax}$ values: (1) change in plant types among C_3 communities (e.g., angiosperms vs. gymnosperms), (2) lessening of water stress conditions because of climate change, and (3) change in the proportion of C_3 and C_4 plants.

Carbon isotope discrimination varies among taxonomic groups due to different water use efficiency and growth strategies (Brooks et al., 1997; Diefendorf and Freimuth, 2017). A change in $\delta^{13}C_{wax}$ values may be a signal of the ecological shift within the C_3 plants. For example, $\varepsilon_{CO2\text{-}wax}$ of conifers are >2‰ lower than angiosperms (Diefendorf et al., 2010; Diefendorf et al., 2011), and $\varepsilon_{CO2\text{-}wax}$ values of gymnosperms are more variable among species than at the family level (Sheldon et al., 2020). If the conifers contribution decreases between 16 and 12 Ma in the Hexi Corridor, we would expect to observe a negative shift in $\delta^{13}C_{wax}$ values. However, this scenario is not supported by the palynology study. Pollen data from the nearby LJM section do not show a resolvable change in angiosperms or gymnosperm proportion during 13–11 Ma (Ma, 2005). Hence the change in photosynthetic fractionation among C_3 plant communities is unlikely the cause for $\delta^{13}C_{wax}$ change in CG from 16 Ma to 12 Ma.

Plant carbon isotopic fractionation is strongly influenced by precipitation amount (PPT). The PPT mediates the leaf gas-exchange by controlling stomatal conductance (Farquhar et al., 1989a; Farquhar et al., 1989b; Marshall et al., 2007). A compilation of the global plant dataset shows increasing $\varepsilon_{CO2\text{-}wax}$ values with mean annual precipitation amount (Diefendorf et al., 2010). $\delta^{13}C_{wax}$ values would decrease with increasing precipitation amount due to reduced water stress, and vice versa. Paleoclimatic data from the northern Tibetan Plateau support a generally arid climate during the middle to late Miocene (Miao et al., 2011; Miao et al., 2012). Pollen record from Qaidam Basin shows an increase in xerophytic plants since ca. 18 Ma, indicating a cooling and drying climate trend (Miao et al., 2011). Hence, decreasing $\delta^{13}C_{wax}$ values from 16 Ma to 12 Ma cannot be attributed to the increasing water availability in the Hexi Corridor.

Plants with different photosynthetic pathways (e.g., C_3 and C_4 pathways) produce distinct carbon isotopic signatures (Diefendorf and Freimuth, 2017). C_4 plants predominantly produce long-chain C_{31} and C_{33} *n*-alkanes, with a mean $\varepsilon_{CO2\text{-}wax}$ value of -26.5 ± 3‰ for C_3 plants and -13.7 ± 2‰ for C_4 plants (Tipple and Pagani, 2010; Jia et al., 2012). Late Holocene $\delta^{13}C_{wax}$ values (−32‰) from Lake Qinghai indicate a C_3 plant-dominated ecosystem (Thomas et al., 2014). $\delta^{13}C_{wax}$ values of CG section between 16 and 12 Ma (Fig. 5A) are higher than the Lake Qinghai $\delta^{13}C_{wax}$ values by ~4‰, indicating the presence of C_4 plant in the Hexi Corridor during the middle-late Miocene. Pollen records from the LJM section identify that herbaceous plant *Artemisiaepollenites* and *Chenopodipollis* are predominant between 13 and 11.15 Ma (Ma, 2005). C_4 Chenopodiaceae species that are abundant in saline and arid Central Asia desert and steppe regions (Pyankov et al., 2000; Lu et al., 2018) might also grow in the Hexi Corridor during the late Miocene. We calculated the contribution of C_4 plants using $\varepsilon_{CO2\text{-}wax}$ of nC_{31} alkanes from Hexi Corridor records from modern end members using Eq. (4) (Fig. 4). The reconstructed C_4 plant proportion from the CG section decrease by ~20% from 16 Ma to 12 Ma (Fig. 4A). The mean C_4 plant proportions in CG, LJM, and WSS sections vary between 0 and 15% after 12 Ma (Fig. 4A-C). C_4 plants have the advantage of adapting to warm growing season temperatures (Ehleringer et al., 1997). Declined global temperature (Zachos et al., 2001) is likely to reduce C_4 plants since the middle Miocene Climate Optimum.

$\delta^{13}C_{wax}$ record from the North Pacific sediments supports a decrease in C_4 plant from ~16% to 10% between 12 Ma and 8 Ma in the sediment source area (northern Tibetan Plateau) (Jia et al., 2012). The decline in the North Pacific record has been interpreted to indicate a cold and arid climate in the northern Tibetan Plateau due to the tectonic uplift and post-middle Miocene global cooling. The $\delta^{13}C_{wax}$ of nC_{31} alkanes from the Qaidam Basin, despite a significant difference in elevation (>1000 m) compared to the Hexi Corridor, shows a contemporaneous negative shift by ~3‰ (Wu et al., 2019). Our calculation shows that this negative shift is equivalent to a ~ 19% decrease in the C_4 plant (Fig. 4D). Apatite fission-track and (U—Th)/He ages, seismic profile interpretations, and magnetostratigraphy and basin analysis studies captured the rapid uplift in the northern Tibetan Plateau since the middle Miocene (Zheng et al., 2006; Ritts et al., 2008; Yin et al., 2008; Clark et al., 2010; Chang et al., 2015; Wang et al., 2016). Hexi Corridor is the foreland basin and located at the geographical lowlands. The reconstructions for the hinterland of intermontane Qaidam Basin and the foreland basin of Hexi Corridor both capture the decline of C_4 plants, indicating that it is the global cooling rather than the tectonism that drove this paleoecological shift.

5.3. Stable hydroclimate in the Hexi corridor during the late Miocene

$\delta^{13}C_{wax}$ records since 12 Ma mainly archive the changes in atmospheric $\delta^{13}C$ values and paleoclimate in the Hexi Corridor. $\delta^{13}C_{wax}$ values of LJM and WSS sections (Fig. 5A) show ~1.5‰ negative shift since 12 Ma, which is consistent with 1‰ decrease in $\delta^{13}C$ values of the atmospheric CO_2 ($\delta^{13}C_{atm}$) during the same period (Fig. 4E) (Tipple et al., 2010). Given that variation of Hexi Corridor $\delta^{13}C_{wax}$ values resemble the trend of $\delta^{13}C_{atm}$ values during the middle and late Miocene, the decrease in $\delta^{13}C_{wax}$ values reflects the change in $\delta^{13}C_{atm}$ values after 12 Ma. We calculated $\varepsilon_{CO2\text{-}wax}$ of CG, LJM, and WSS sections by subtracting the effect on the $\delta^{13}C_{wax}$ values due to $\delta^{13}C_{atm}$ variation (Fig. 5B). Because C_4 plant is rare (average of 10%) in the Hexi Corridor since ~12 Ma based on our reconstructions (Fig. 4), the calculated $\varepsilon_{CO2\text{-}wax}$ values mainly reflect carbon isotope fractionation of C_3 plant in response to hydrological change (e.g., precipitation and evaporation). Mean $\varepsilon_{CO2\text{-}wax}$ value is ~27‰ for LJM, ~26‰ for WSS, and ~ 25‰ for CG sections. $\varepsilon_{CO2\text{-}wax}$ values of three sections in the Hexi Corridor vary within an amplitude of 1–2‰ since 12 Ma, suggesting a relatively stable hydrological condition. This inference is supported by relatively invariant $\delta^{18}O$ and $\delta^{13}C$ values of carbonate in the LJM, WSS, and CG sections (Fig. 5C and D; except two data points at the CG section)). Our new $\delta^{18}O$ and $\delta^{13}C$ values of carbonate are consistent with previous stable isotopic records from the Hexi Corridor (Kent-Corson et al., 2009).

5.4. Uplift-driven isolation of Qaidam Basin and enhanced aridity

Paleoclimate studies from the Qaidam Basin show that climate has become increasingly arid since the middle Miocene, which is concurrent with high elevation obtained in the northern Tibetan Plateau (Bovet et al., 2009; Zhuang et al., 2014; Zuza et al., 2016; Zhuang et al., 2019). Calculated $\varepsilon_{CO2\text{-}wax}$ values from QGQ and HGZ sections in the western Qaidam (Fig. 5E) decrease by ~2‰ since ~12 Ma. The decrease in $\varepsilon_{CO2\text{-}wax}$ is unlikely to reflect an increase in C_4 plants because the cooling climate since ~15 Ma do not favor for C_4 plants. Water stress has been recognized as a strong control on carbon discrimination of C_3 plants (Diefendorf and Freimuth, 2017). Water availability influences the plant's stomal conductance and CO_2 uptake during photosynthesis, which affects carbon isotope fractionation. Decreasing $\varepsilon_{CO2\text{-}wax}$ since 12 Ma in the Qaidam Basin likely reflects enhanced evaporation and water stress.

$\delta^{18}O$ records (Fig. 5F) of fluvial and lacustrine carbonates (Kent-Corson et al., 2009; Zhuang et al., 2011) show the similar trends as the calculated $\varepsilon_{CO2\text{-}wax}$ records (Wu et al., 2019) in the Qaidam Basin and support a generally arid climate after the middle to late Miocene. Variations in $\delta^{18}O$ trends among sites in the Qaidam Basin may be attributed to the local tectonic, environmental settings, and/or comparison uncertainties in ages (Kent-Corson et al., 2009). The enhanced dry climate in the Qaidam Basin is distinguished from the stable hydroclimate condition in the adjacent Hexi Corridor during the same interval (Fig. 5). Especially, the $\delta^{18}O$ values in the Qaidam records (Kent-Corson et al., 2009) resemble those in the Hexi Corridor, even though the elevation of the Qaidam Basin is more than 1000 m higher than that of the Hexi Corridor (Fig. 5D and F). $\delta^{18}O$ values are supposed to become more negative as increasing elevation since heavier oxygen isotope (^{18}O) become progressively depleted during rainfall (Garzione et al., 2000; Poage and Chamberlain, 2001; Rowley et al., 2001). Modern precipitation $\delta^{18}O$ values in the Qaidam (meteorological station in Delingha) is lower than $\delta^{18}O$ values in Hexi Corridor (meteorological station in Zhangye) (Tian et al., 2003; IAEA/WMO, 2006) (Fig. S5). Given that these two sites have similar mean annual precipitation (Fig. 1), lower precipitation $\delta^{18}O$ values in the Qaidam is likely to result from the higher elevation. We argue that similar mean $\delta^{18}O$ values in the Qaidam Basin and Hexi Corridor since 12 Ma imply that isotopic depletion due to higher elevation in the Qaidam Basin has been reversed by the isotopic enrichment caused by drier climate on the surface water.

The contrasting climatic patterns in the Hexi Corridor and the Qaidam Basin are related to their tectonic settings. Increasing evidence suggests a major uplift and outward expansion of the northern Tibetan Plateau during the middle to late Miocene, as suggested by the following structural, stable isotope, biomarker, and thermochronological studies. Provenance analysis of Miocene granitic clasts north of Altyn Tagh fault suggests a reduced slip rate and a transition of tectonic activation from lateral extrusion to the distributed crustal thickening since the end of early Miocene (Yue et al., 2004). Sedimentary records from Hexi Corridor suggest that high energy deposition and northeast-trending paleocurrent initiate since ca. 13 Ma, indicating crustal shortening in the North Qilian Shan before the late Miocene (Bovet et al., 2009). These findings are consistent with apatite fission-track studies showing rapid cooling in the North Qilian Shan during 20–10 Ma (George et al., 2001; Zheng et al., 2010). Nd isotopic record from North Pacific suggests increasing input of Asian dust sediment since 15 Ma, resulting from accelerated exhumation on northern Tibetan Plateau induced by surface uplift (Li et al., 2011). Stable isotopic studies from Qaidam, Linxia, and Xunhua Basins suggest surface uplift of northeastern Tibetan Plateau between ca. 15–11 Ma (Hough et al., 2011; Zhuang et al., 2014). Recent detrital zircon U—Pb and paleothermometry data show that the northern Tibetan Plateau's high topography has gained by ca. 8 Ma (Chen et al., 2019; Zhuang et al., 2019). We argue that Qaidam Basin has encountered more substantial evaporation and less precipitation than the Hexi Corridor since the northern Tibetan Plateau was uplifted at the middle to late Miocene. The uplift of basin-bounding ranges in the northern Tibetan Plateau (Altyn Shan and Qilian Shan) has intensified arid climate and hydrological isolation of the Qaidam Basin by either blocking Westerlies air mass or reducing moisture from the Atlantic and Arctic. Hence, tectonic forcing plays a pivotal role in enhancing the Qaidam Basin's aridity during the late Miocene.

5.5. Intra-basinal variation in hydrology and ecology in the Hexi Corridor

$\delta^{13}C_{wax}$ and $\delta^{18}O$ records in the Hexi Corridor show persistent intra-basinal offsets since ca. 12 Ma (Figs. 5A and 6), reflecting distinguished hydrological and vegetation patterns within different parts of the basin. Even though all three sections show similar isotopic trends, the $\delta^{13}C_{wax}$ values of LJM are overall more negative than those of WSS by ~1‰ and are lower than those of CG by ~1.5‰ (Fig. 5A). The mean $\delta^{18}O$ values in the LJM (−8.7‰) is lower than in the WSS (−8.1‰) and CG (−7.5‰) (Fig. 6). The offsets in mean $\delta^{18}O$ values indicate local environmental features– orographic effect. The orographic rainfall effect demonstrates that more precipitation occurs in the mountain front and diminishes toward the basin's center. Our field observation along the transection reveals a transition in vegetation types from patches of forests at LJM near the Qilian Shan slope, shrubs in the WSS to sparse grasses in the CG at the center of the Hexi Corridor Basin (Fig. 6). $\delta^{18}O$ values would become more depleted due to increased precipitation as approaching the North Qilian Shan front. LJM is closest to the North Qilian Shan comparing with the other two sections. Thus, it could receive more precipitation and the lowest mean $\delta^{18}O$ values. Contrarily, CG is at the northern margin of the western Hexi Corridor. Less rainfall and more enhanced evaporation and recycling of moistures can lead to more positive $\delta^{18}O$ values. $\delta^{13}C_{wax}$ records support the intra-basinal variation in hydrology and ecology. The highest $\delta^{13}C_{wax}$ values in CG among three stratigraphic sections likely indicate a high water-stressed environment. In addition to hydrology, higher $\delta^{13}C_{wax}$ values in CG may imply more abundant C_4 plants because C_4 plants are more adaptable at low elevations.

6. Conclusions

We use leaf wax carbon isotopes and carbonate oxygen isotopes to reconstruct post-middle Miocene paleoecology and paleoclimate from sedimentary successions in the Hexi Corridor. Isotopic records show a decline in the abundance of C_4 plants between ca. 16–12 Ma due to the post middle Miocene global cooling. The stable carbon isotope discrimination ($\varepsilon_{CO2\text{-}wax}$) and carbonate oxygen and carbon isotopes show disparate trends in the foreland basin of the Hexi Corridor and the intermontane Qaidam Basin since 12 Ma. We attribute the differences to the uplift-associated basin isolation of the Qaidam Basin, a result of tectonism since the mid-late Miocene that is consistent with regional geological studies. Intra-basinal variations on isotopic values within the Hexi Corridor reflect local environmental features associated with orographic precipitation and altitude effect.

Declaration of Competing Interest

The authors declare that they have no known competing financial interests or personal relationships that could have appeared to influence the work reported in this paper.

Acknowledgments

We thank two anonymous reviewers for their thorough and constructive comments that greatly improve the quality of the paper. We thank Amber Ellwood for her laboratory assistance. The project is supported by the US National Science Foundation (NSF) Grant EAR 2022282 to Zhuang.

Appendix A. Supplementary data

Supplementary data to this article can be found online at https://doi.org/10.1016/j.palaeo.2021.110578.

References

An, Z., 1998. New Viewpoint of Forming Laojunmiao Oilfield, 19. Petroleum Industry Press, pp. 265–269 no. 4. (in Chinese with English abstract).

An, Z., 2014. Late Cenozoic Climate Change in Asia: Loess, Monsoon and Monsoon-Arid Environment Evolution. Springer Science & Business Media.

An, Z., Kutzbach, J.E., Prell, W.L., Porter, S.C., 2001. Evolution of Asian monsoons and phased uplift of the Himalaya–Tibetan plateau since Late Miocene times. Nature 411 (6833), 62–66.

Andersson, R.A., Meyers, P.A., 2012. Effect of climate change on delivery and degradation of lipid biomarkers in a Holocene peat sequence in the Eastern European Russian Arctic. Org. Geochem. 53, 63–72.

Ankit, Y., Mishra, P.K., Kumar, P., Jha, D.K., Kumar, V.V., Ambili, V., Anoop, A., 2017. Molecular distribution and carbon isotope of n -alkanes from Ashtamudi Estuary, South India: assessment of organic matter sources and paleoclimatic implications. Mar. Chem. 196, 62–70.

Araguás-Araguás, L., Froehlich, K., Rozanski, K., 1998. Stable isotope composition of precipitation over southeast Asia. J. Geophys. Res.-Atmos. 103 (D22), 28721–28742.

Bakhtiari, A.R., Zakaria, M.P., Yaziz, M.I., Lajis, M.N.H., Bi, X., Shafiee, M.M., Sakari, M., 2010. Distribution of PAHs and n-alkanes in Klang River surface sediments, Malaysia. Pertanika J. Sci. Technol. 18 (1), 167–179.

Bershaw, J., Penny, S.M., Garzione, C.N., 2012. Stable isotopes of modern water across the Himalaya and eastern Tibetan Plateau: implications for estimates of paleoelevation and paleoclimate. J. Geophys. Res.-Atmos. 117.

Boos, W.R., Kuang, Z., 2010. Dominant control of the South Asian monsoon by orographic insulation versus plateau heating. Nature 463 (7278), 218–U102.

Bovet, P.M., Ritts, B.D., Gehrels, G., Abbink, A.O., Darby, B., Hourigan, J., 2009. Evidence of Miocene crustal shortening in the North Qilian Shan from Cenozoic stratigraphy of the western Hexi Corridor, Gansu Province, China. Am. J. Sci. 309 (4), 290–329.

Brittingham, A., Hren, M.T., Hartman, G., 2017. Microbial alteration of the hydrogen and carbon isotopic composition of n -alkanes in sediments. Org. Geochem. 107, 1–8.

Brooks, J.R., Flanagan, L.B., Buchmann, N., Ehleringer, J.R., 1997. Carbon isotope composition of boreal plants: functional grouping of life forms. Oecologia 110 (3), 301–311.

Cerling, T.E., Harris, J.M., MacFadden, B.J., Leakey, M.G., Quade, J., Eisenmann, V., Ehleringer, J.R., 1997. Global vegetation change through the Miocene/Pliocene boundary. Nature 389 (6647), 153–158.

ChaIneau, C.-H., Morel, J.-L., Oudot, J., 1995. Microbial degradation in soil microcosms of fuel oil hydrocarbons from drilling cuttings. Environ. Sci. Technol. 29 (6), 1615–1621.

Chang, H., Li, L., Qiang, X., Garzione, C.N., Pullen, A., An, Z., 2015. Magnetostratigraphy of Cenozoic deposits in the western Qaidam Basin and its implication for the surface uplift of the northeastern margin of the Tibetan Plateau. Earth Planet. Sci. Lett. 430, 271–283.

Chen, C., Bai, Y., Fang, X., Guo, H., Meng, Q., Zhang, W., Zhou, P., Murodov, A., 2019. A Late Miocene Terrestrial Temperature History for the Northeastern Tibetan Plateau's Period of Tectonic Expansion. Geophys. Res. Lett. 46 (14), 8375–8386.

Clark, M.K., Farley, K.A., Zheng, D., Wang, Z., Duvall, A.R., 2010. Early Cenozoic faulting of the northern Tibetan Plateau margin from apatite (U-Th)/He ages. Earth Planet. Sci. Lett. 296 (1–2), 78–88.

Collatz, G.J., Berry, J.A., Clark, J.S., 1998. Effects of climate and atmospheric CO2 partial pressure on the global distribution of C-4 grasses: present, past, and future. Oecologia 114 (4), 441–454.

Collister, J.W., Rieley, G., Stern, B., Eglinton, G., Fry, B., 1994. Compound-specific delta-C-13 analyses of leaf lipids from plants with differing carbon-dioxide metabolisms. Org. Geochem. 21 (6–7), 619–627.

Dai, S., Fang, X., Song, C., Gao, J., Gao, D., Li, J., 2005. Early tectonic uplift of the northern Tibetan Plateau. Chin. Sci. Bull. English Ed. 50 (15), 1642.

Dettman, D.L., Kohn, M.J., Quade, J., Ryerson, F., Ojha, T.P., Hamidullah, S., 2001. Seasonal stable isotope evidence for a strong Asian monsoon throughout the past 10.7 my. Geology 29 (1), 31–34.

Dettman, D.L., Fang, X., Garzione, C.N., Li, J., 2003. Uplift-driven climate change at 12 Ma: a long δ18O record from the NE margin of the Tibetan plateau. Earth Planet. Sci. Lett. 214 (1–2), 267–277.

Diefendorf, A.F., Freimuth, E.J., 2017. Extracting the most from terrestrial plant-derived n-alkyl lipids and their carbon isotopes from the sedimentary record: a review. Org. Geochem. 103, 1–21.

Diefendorf, A.F., Mueller, K.E., Wing, S.L., Koch, P.L., Freeman, K.H., 2010. Global patterns in leaf 13C discrimination and implications for studies of past and future climate. Proc. Natl. Acad. Sci. 107 (13), 5738–5743.

Diefendorf, A.F., Freeman, K.H., Wing, S.L., Graham, H.V., 2011. Production of n-alkyl lipids in living plants and implications for the geologic past. Geochim. Cosmochim. Acta 75 (23), 7472–7485.

Diefendorf, A.F., Sberna, D.T., Taylor, D.W., 2015. Effect of thermal maturation on plant-derived terpenoids and leaf wax n-alkyl components. Org. Geochem. 89-90, 61–70.

Dupont, L.M., Behling, H., Jahns, S., Marret, F., Kim, J.H., 2007. Variability in glacial and Holocene marine pollen records offshore from west southern Africa. Veg. Hist. Archaeobotany 16 (2–3), 87–100.

Dupont-Nivet, G., Krijgsman, W., Langereis, C.G., Abels, H.A., Dai, S., Fang, X., 2007. Tibetan plateau aridification linked to global cooling at the Eocene-Oligocene transition. Nature 445 (7128), 635–638.

Edwards, E.J., Smith, S.A., 2010. Phylogenetic analyses reveal the shady history of C-4 grasses. Proc. Natl. Acad. Sci. U. S. A. 107 (6), 2532–2537.

Edwards, E.J., Osborne, C.P., Stroemberg, C.A.E., Smith, S.A., Bond, W.J., Christin, P.-A., Cousins, A.B., Duvall, M.R., Fox, D.L., Freckleton, R.P., Ghannoum, O., Hartwell, J., Huang, Y., Janis, C.M., Keeley, J.E., Kellogg, E.A., Knapp, A.K., Leakey, A.D.B., Nelson, D.M., Saarela, J.M., Sage, R.F., Sala, O.E., Salamin, N., Still, C.J., Tipple, B., Consortium, C.G., 2010. The origins of C-4 grasslands: integrating evolutionary and ecosystem science. Science 328 (5978), 587–591.

Eglinton, G., Hamilton, R.J., 1967. Leaf epicuticular waxes. Science 156 (3780), 1322–+.

Eglinton, T., Douglas, A., Rowland, S., 1988. Release of aliphatic, aromatic and sulphur compounds from Kimmeridge kerogen by hydrous pyrolysis: A quantitative study. Org. Geochem. 13 (4–6), 655–663.

Ehleringer, J.R., Cerling, T.E., Helliker, B.R., 1997. C-4 photosynthesis, atmospheric CO2 and climate. Oecologia 112 (3), 285–299.

Fang, X., 2005. Magnetostratigraphy of the late Cenozoic Laojunmiao anticline in the northern Qilian Mountains and its implications for the northern Tibetan Plateau uplift. Sci. China Ser. D 48 (7).

Fang, J., Wu, F., Xiong, Y., Li, F., Du, X., An, D., Wang, L., 2014. Source characterization of sedimentary organic matter using molecular and stable carbon isotopic composition of n-alkanes and fatty acids in sediment core from Lake Dianchi, China. Sci. Total Environ. 473-474, 410–421.

Farquhar, G.D., O'Leary, M.H., Berry, J.A., 1982. On the relationship between carbon isotope discrimination and the intercellular carbon dioxide concentration in leaves. Funct. Plant Biol. 9 (2), 121–137.

Farquhar, G., Hubick, K., Condon, A., Richards, R., 1989a. Carbon isotope fractionation and plant water-use efficiency. In: Stable Isotopes in Ecological Research. Springer, pp. 21–40.

Farquhar, G.D., Ehleringer, J.R., Hubick, K.T., 1989b. Carbon isotope discrimination and photosynthesis. Annu. Rev. Plant Physiol. Plant Mol. Biol. 40, 503–537.

Garzione, C.N., Quade, J., DeCelles, P.G., English, N.B., 2000. Predicting paleoelevation of Tibet and the Himalaya from δ 18 O vs. altitude gradients in meteoric water across the Nepal Himalaya. Earth Planet. Sci. Lett. 183 (1), 215–229.

GBGMR, 1989. Regional Geology of Gansu Province. Geological Publishing House, Beijing.

George, A.D., Marshallsea, S.J., Wyrwoll, K.H., Chen, J., Lu, Y.C., 2001. Miocene cooling in the northern Qilian Shan, northeastern margin of the Tibetan Plateau, revealed by apatite fission-track and vitrinite-reflectance analysis. Geology 29 (10), 939–942.

Hou, M., Zhuang, G., Ji, J., Xiang, S., Kong, W., Cui, X., Wu, M., Hren, M., 2020. Profiling interactions between the Westerlies and Asian summer monsoons since 45 ka: insights from biomarker, isotope, and numerical modeling studies in the Qaidam Basin. GSA Bull. 133 (7–8), 1531–1541.

Hough, B.G., Garzione, C.N., Wang, Z., Lease, R.O., Burbank, D.W., Yuan, D., 2011. Stable isotope evidence for topographic growth and basin segmentation: implications for the evolution of the NE Tibetan Plateau. Geol. Soc. Am. Bull. 123 (1–2), 168–185.

Huang, Y., Clemens, S.C., Liu, W., Wang, Y., Prell, W.L., 2007. Large-scale hydrological change drove the late Miocene C4 plant expansion in the Himalayan foreland and Arabian Peninsula. Geology 35 (6), 531–534.

IAEA/WMO, 2006. Global Network of Isotopes in Precipitation: The GNIP Database. Accessible at. http://isohis.iaea.org.

Jia, G., Li, Z., Peng, P.a., Zhou, L., 2012. Aeolian n-alkane isotopic evidence from North Pacific for a Late Miocene decline of C4 plant in the arid Asian interior. Earth Planet. Sci. Lett. 321, 32–40.

Kara-Gülbay, R., Yaylalı-Abanuz, G., Korkmaz, S., Erdoğan, M., Hoş-Çebi, F., Çevik, S., Ağırman-Aktürk, E., 2019. Organic matter type, maturity, depositional environmental characteristics, and liquid hydrocarbon potential of late carboniferous Kozlu Bituminous coal and coaly shale beds (Zonguldak-Amasra Basin, NW Anatolia, Turkey): an application of biomarker geochemistry. Energy Fuel 33 (10), 9491–9509.

Kennicutt II, M., Barker, C., Brooks, J., DeFreitas, D., Zhu, G., 1987. Selected organic matter source indicators in the Orinoco, Nile and Changjiang deltas. Org. Geochem. 11 (1), 41–51.

Kent-Corson, M.L., Ritts, B.D., Zhuang, G., Bovet, P.M., Graham, S.A., Chamberlain, C.P., 2009. Stable isotopic constraints on the tectonic, topographic, and climatic evolution of the northern margin of the Tibetan Plateau. Earth Planet. Sci. Lett. 282 (1–4), 158–166.

Kutzbach, J.E., Guetter, P.J., Ruddiman, W.F., Prell, W.L., 1989. Sensitivity of climate to Late Cenozoic uplift in Southern Asia and the American West - numerical experiments. J. Geophys. Res.-Atmos. 94 (D15), 18393–18407.

Li, L., Garzione, C.N., 2017. Spatial distribution and controlling factors of stable isotopes in meteoric waters on the Tibetan Plateau: implications for paleoelevation reconstruction. Earth Planet. Sci. Lett. 460, 302–314.

Li, G., Pettke, T., Chen, J., 2011. Increasing Nd isotopic ratio of Asian dust indicates progressive uplift of the north Tibetan Plateau since the middle Miocene. Geology 39 (3), 199–202.

Li, L., Garzione, C.N., Pullen, A., Chang, H., 2016. Early–middle Miocene topographic growth of the northern Tibetan Plateau: stable isotope and sedimentation evidence from the southwestern Qaidam basin. Palaeogeogr. Palaeoclimatol. Palaeoecol. 461, 201–213.

Lu, K.Q., Li, M., Wang, G.H., Xu, L.S., Ferguson, D.K., Trivedi, A., Xuan, J., Feng, Y., Li, J. F., Xie, G., Yao, Y.F., Wang, Y.F., 2018. New pollen classification of Chenopodiaceae

for exploring and tracing desert vegetation evolution in eastern arid central Asia. J. Syst. Evol. 57 (2), 190–199.
Lu, Q., Qin, S., Xu, F., Chang, X., Wang, W., 2021. Maceral and Organic Geochemical Characteristics of the Late Permian Coals from Yueliangtian Mine, Guizhou, Southwestern China. ACS Omega 6 (4), 3149–3163.
Ma, Y., 2005. The vegetation and climate change during Neocene and Early Quaternary in Jiuxi Basin, China. Sci. China Ser. D 48 (5).
Marshall, J.D., Brooks, J.R., Lajtha, K.J.S., i. i. e., and science, e, 2007. Sources of Variation in the Stable Isotopic Composition of Plants, 2, pp. 22–60.
Marzi, R., Torkelson, B.E., Olson, R.K., 1993. A revised carbon preference index. Org. Geochem. 20 (8), 1303–1306.
Metivier, F., Gaudemer, Y., Tapponnier, P., Meyer, B., 1998. Northeastward growth of the Tibet plateau deduced from balanced reconstruction of two depositional areas: the Qaidam and Hexi Corridor basins, China. Tectonics 17 (6), 823–842.
Miao, Y., Fang, X., Herrmann, M., Wu, F., Zhang, Y., Liu, D., 2011. Miocene pollen record of KC-1 core in the Qaidam Basin, NE Tibetan Plateau and implications for evolution of the East Asian monsoon. Palaeogeogr. Palaeoclimatol. Palaeoecol. 299 (1–2), 30–38.
Miao, Y., Herrmann, M., Wu, F., Yan, X., Yang, S., 2012. What controlled Mid–Late Miocene long-term aridification in Central Asia?—Global cooling or Tibetan Plateau uplift: a review. Earth Sci. Rev. 112 (3–4), 155–172.
Molnar, P., Stock, J.M., 2009. Slowing of India's convergence with Eurasia since 20 Ma and its implications for Tibetan mantle dynamics. Tectonics 28.
Molnar, P., England, P., Martinod, J., 1993. Mantle dynamics, uplift of the Tibetan Plateau, and the Indian monsoon. Rev. Geophys. 31 (4), 357–396.
Molnar, P., Boos, W.R., Battisti, D.S., 2010. Orographic controls on climate and paleoclimate of Asia: thermal and mechanical roles for the Tibetan Plateau. Annu. Rev. Earth Planet. Sci. 38, 77–102.
Najman, Y., Appel, E., Boudagher-Fadel, M., Bown, P., Carter, A., Garzanti, E., Godin, L., Han, J., Liebke, U., Oliver, G., Parrish, R., Vezzoli, G., 2010. Timing of India-Asia collision: geological, biostratigraphic, and palaeomagnetic constraints. J. Geophys. Res. 115 (B12).
O'Leary, M.H., 1988. Carbon isotopes in photosynthesis. Bioscience 38 (5), 328–336.
Pagani, M., Freeman, K.H., Arthur, M.A., 1999. Late Miocene atmospheric CO2 concentrations and the expansion of C-4 grasses. Science 285 (5429), 876–879.
Poage, M.A., Chamberlain, C.P., 2001. Empirical relationships between elevation and the stable isotope composition of precipitation and surface waters: considerations for studies of paleoelevation change. Am. J. Sci. 301 (1), 1–15.
Pyankov, V.I., Gunin, P.D., Tsoog, S., Black, C.C., 2000. C 4 plants in the vegetation of Mongolia: their natural occurrence and geographical distribution in relation to climate. Oecologia 123 (1), 15–31.
Ritts, B.D., Yue, Y., Graham, S.A., Sobel, E.R., Abbink, O.A., Stockli, D., 2008. From sea level to high elevation in 15 million years: uplift history of the northern Tibetan Plateau margin in the Altun Shan. Am. J. Sci. 308 (5), 657–678.
Rowley, D.B., Pierrehumbert, R.T., Currie, B.S., 2001. A new approach to stable isotope-based paleoaltimetry: implications for paleoaltimetry and paleohypsometry of the High Himalaya since the Late Miocene. Earth Planet. Sci. Lett. 188 (1–2), 253–268.
Ruddiman, W.F., Kutzbach, J.E., 1989. Forcing of Late Cenozoic northern hemisphere climate by plateau uplift in Southern Asia and the American West. J. Geophys. Res.-Atmos. 94 (D15), 18409–18427.
Selley, R.C., 1998. Elements of Petroleum Geology. Gulf Professional Publishing.
Sheldon, N.D., Smith, S.Y., Stein, R., Ng, M., 2020. Carbon isotope ecology of gymnosperms and implications for paleoclimatic and paleoecological studies. Glob. Planet. Chang. 184.
Simoneit, B.R., 1994. Lipid/bitumen maturation by hydrothermal activity in sediments of Middle Valley. Leg 139.
Sparks, J.P., Ehleringer, J.R., 1997. Leaf carbon isotope discrimination and nitrogen content for riparian trees along elevational transects. Oecologia 109 (3), 362–367.
Strömberg, C.A., 2011. Evolution of grasses and grassland ecosystems. Annu. Rev. Earth Planet. Sci. 39, 517–544.
Tang, Z., Ding, Z., White, P.D., Dong, X., Ji, J., Jiang, H., Luo, P., Wang, X., 2011. Late Cenozoic central Asian drying inferred from a palynological record from the northern Tian Shan. Earth Planet. Sci. Lett. 302 (3–4), 439–447.
Tapponnier, P., Zhiqin, X., Roger, F., Meyer, B., Arnaud, N., Wittlinger, G., Jingsui, Y., 2001. Oblique stepwise rise and growth of the Tibet Plateau. Science 294 (5547), 1671–1677.
Thomas, E.K., Huang, Y., Morrill, C., Zhao, J., Wegener, P., Clemens, S.C., Colman, S.M., Gao, L., 2014. Abundant C4 plants on the Tibetan Plateau during the Lateglacial and early Holocene. Quat. Sci. Rev. 87, 24–33.
Tian, L., Masson-Delmotte, V., Stievenard, M., Yao, T., Jouzel, J., 2001. Tibetan Plateau summer monsoon northward extent revealed by measurements of water stable isotopes. J. Geophys. Res.-Atmos. 106 (D22), 28081–28088.
Tian, L., Yao, T., Schuster, P.F., White, J.W.C., Ichiyanagi, K., Pendall, E., Pu, J., Wu, Y., 2003. Oxygen-18 concentrations in recent precipitation and ice cores on the Tibetan Plateau. J. Geophys. Res.-Atmos. 108 (D9).
Tipple, B.J., Pagani, M., 2007. The early origins of terrestrial C4 photosynthesis. Annu. Rev. Earth Planet. Sci. 35, 435–461.
Tipple, Brett J., Pagani, Mark, 2010. A 35Myr North American leaf-wax compound-specific carbon and hydrogen isotope record: implications for C 4 grasslands and hydrologic cycle dynamics. Earth Planet. Sci. Lett. 299 (1), 250–262.
Tipple, B.J., Meyers, S.R., Pagani, M., 2010. Carbon isotope ratio of Cenozoic CO2: a comparative evaluation of available geochemical proxies. Paleoceanography 25 (3).
Wang, W., Zhang, P., Pang, J., Garzione, C., Zhang, H., Liu, C., Zheng, D., Zheng, W., Yu, J., 2016. The Cenozoic growth of the Qilian Shan in the northeastern Tibetan Plateau: a sedimentary archive from the Jiuxi Basin. J. Geophys. Res. Solid Earth 121 (4), 2235–2257.
Wang, S., Liu, G., Yuan, Z., Da, C., 2018. n-Alkanes in sediments from the Yellow River Estuary, China: occurrence, sources and historical sedimentary record. Ecotoxicol. Environ. Saf. 150, 199–206.
Wang, X., Carrapa, B., Sun, Y., Dettman, D.L., Chapman, J.B., Caves Rugenstein, J.K., Clementz, M.T., DeCelles, P.G., Wang, M., Chen, J., 2020. The role of the westerlies and orography in Asian hydroclimate since the late Oligocene. Geology 48 (7), 728–732.
Wu, M., Zhuang, G., Hou, M., Miao, Y., 2019. Ecologic shift and aridification in the northern Tibetan Plateau revealed by leaf wax n-alkane δ2H and δ13C records. Palaeogeogr. Palaeoclimatol. Palaeoecol. 514, 464–473.
Yin, A., Dang, Y.Q., Zhang, M., Chen, X.H., McRivette, M.W., 2008. Cenozoic tectonic evolution of the Qaidam basin and its surrounding regions (Part 3): structural geology, sedimentation, and regional tectonic reconstruction. Geol. Soc. Am. Bull. 120 (7–8), 847–876.
Yue, Y., Ritts, B.D., Graham, S.A., Wooden, J.L., Gehrels, G.E., Zhang, Z., 2004. Slowing extrusion tectonics: lowered estimate of post-Early Miocene slip rate for the Altyn Tagh fault. Earth Planet. Sci. Lett. 217 (1–2), 111–122.
Zachos, J., Pagani, M., Sloan, L., Thomas, E., Billups, K., 2001. Trends, rhythms, and aberrations in global climate 65 Ma to present. Science 292 (5517), 686–693.
Zhao, Z., Fang, X., Li, J., 2001. Late Cenozoic magnetic polarity stratigraphy in the Jiudong Basin, northern Qilian Mountain. Sci. China Ser. D Earth Sci. 44 (1), 243–250.
Zheng, D., Zhang, P.-Z., Wan, J., Yuan, D., Li, C., Yin, G., Zhang, G., Wang, Z., Min, W., Chen, J., 2006. Rapid exhumation at ~8 Ma on the Liupan Shan thrust fault from apatite fission-track thermochronology: Implications for growth of the northeastern Tibetan Plateau margin. Earth Planet. Sci. Lett. 248 (1–2), 198–208.
Zheng, D., Clark, M.K., Zhang, P., Zheng, W., Farley, K.A., 2010. Erosion, fault initiation and topographic growth of the North Qilian Shan (northern Tibetan Plateau). Geosphere 6 (6), 937–941.
Zhuang, G., Hourigan, J.K., Koch, P.L., Ritts, B.D., Kent-Corson, M.L., 2011. Isotopic constraints on intensified aridity in Central Asia around 12 Ma. Earth Planet. Sci. Lett. 312 (1–2), 152–163.
Zhuang, G., Brandon, M.T., Pagani, M., Krishnan, S., 2014. Leaf wax stable isotopes from Northern Tibetan Plateau: implications for uplift and climate since 15 Ma. Earth Planet. Sci. Lett. 390, 186–198.
Zhuang, G., Zhang, Y.G., Hourigan, J., Ritts, B., Hren, M., Hou, M., Wu, M., Kim, B., 2019. Microbial and geochronologic constraints on the Neogene paleotopography of northern Tibetan Plateau. Geophys. Res. Lett. 46 (3), 1312–1319.
Zuza, A.V., Cheng, X., Yin, A., 2016. Testing models of Tibetan Plateau formation with Cenozoic shortening estimates across the Qilian Shan–Nan Shan thrust belt. Geosphere 12 (2), 501–532.